Journal of Porous Materials (2023) 30:797–810
https://doi.org/10.1007/s10934-022-01372-5

Sucrose-based activated carbon foams as an electrode active material for supercapacitors

Zehra Özçifçi[1] · Mehmet Ali Özşanlı[2] · Hakkı Türker Akçay[1] · Tuğrul Yumak[2]

Accepted: 17 October 2022 / Published online: 11 November 2022

Abstract
Activated carbon foams (ACFs) have been successfully prepared by foaming sucrose with Zn nitrate and further chemical activation with H_3PO_4. The effect of the foaming agent (Zn) concentration and the activation temperature on the surface chemistry, porosity, and morphology were investigated. The ACFs reveal high specific surface area, non-uniform variable porous structure, and high oxygen content. The ACFs represent high specific capacitance and very low equivalent serial resistance (ESR) values as electrode material. The ACF obtained at 600 °C has a specific capacitance of 205.4 F/g at 1 A/g constant current density. The pseudocapacitive contribution of oxygen-containing surface functional groups was proved by CV curves at slow scan rates. The high performance of the ACFs may be attributed not only to the high surface area, and hetero-atom-containing SGFs but also to the unique surface morphology which originated from the release of gaseous products during the foaming process.

Keywords Bio-based porous activated carbon foams · Energy storage · Supercapacitor · Porous materials characterization

1 Introduction

Activated carbon foams (ACFs) are ultra-light porous carbon materials with a sponge-like structure that are used in many applications thanks to their low density, high surface area, hydrophobic structure, thermal properties, electrical, and electrochemical properties [1]. ACFs are widely found in the wearing parts of thermal protection systems, high-temperature thermal insulation, sensor applications, sound insulation, catalyst support, energy storage systems, adsorbent materials, etc. [2]. ACFs are divided into two groups: graphitic carbon and non-graphitic carbon. Graphitic foams are obtained by the carbonization/graphitization processes of the foamed fossil fuel precursors such as coal, coal tar, and petroleum. Glassy carbon foams, also known as non-graphitic carbon foams, are obtained by the carbonization process of high carbon content polymers precursors such as phenol–formaldehyde, resorcinol formaldehyde, polyimide [3]. The rapid depletion of fossil fuels led to the use of bio-based materials such as sugar derivatives, tannin, and corn stoves as carbon sources due to their several advantages. Bio-based carbon sources can be converted into high-value-added products especially biochar, hydrochar, and activated carbon via well-known thermal treatment techniques. They have several advantages over fossil-fuel-based ones such as being environmentally friendly, low-cost, and high-performance/efficient for a wide range of applications. Besides, the usage of bio-sources leads to a significant reduction in environmental pollution and helps to lower the CO_2 emission into the atmosphere by carbon cycle [4, 5]. Among bio-based carbon sources, sugar which is widely used in the production of micro and mesoporous carbons has been studied by many researchers for various applications [6, 7]. Sugar with a global market value of USD 37.62 billion in 2021 is a crucial material for the food industry. Nearly 110 countries produce sugar from either cane or beet, and the top ten producing countries (India, Brazil, Thailand, China, the US, Mexico, Russia, Pakistan, France, and Australia) accounted for nearly 70% of global output. In the 2022/2023 crop year, global sugar production is expected

Zehra Özçifçi and Mehmet Ali Özşanlı have contributed equally to this work.

✉ Tuğrul Yumak
tyumak@sinop.edu.tr; tugrulyumak@yahoo.com

[1] Department of Chemistry, Faculty of Arts and Sciences, Recep Tayyip Erdoğan University, Rize, Turkey

[2] Department of Chemistry, Faculty of Arts and Sciences, Sinop University, Sinop, Turkey

to be 182 million metric tons, up 1.7 million tons from the previous year [8].

In recent years, environmental problems caused by the depletion of fossil fuels and global warming, together with the increasing population and developing technology, increase the demand for clean electricity generation and energy storage devices. Supercapacitors can be divided into two main groups depending on the charge storage mechanism: Electrochemical Double Layer Capacitors (EDLCs) and pseudocapacitors [9]. In EDLC, the energy is stored by pure physical accumulation at the electrode/electrolyte interface by the formation of double-layer ions, whereas in pseudocapacitors, this happens via redox reactions of faradaic materials [10]. Supercapacitors are used instead of and/or complementary to batteries due to the requirement of fast charge–discharge rate, long cycle life, high stability, and high-power density [11]. Carbon-based materials such as graphene, MWCNT, SWCNT, and activated carbons (ACs) are used as electrode materials in EDLCs. The performance of a carbonaceous electrode is affected by various parameters such as the microstructure of the electrolyte, surface chemistry, pore size and distribution, surface area, and pore tortuosity [12]. Pores smaller than the ion size or highly convoluted pores with a bottleneck can prevent electrolyte ions from accessing the surface, resulting in low capacitance and slow frequency response. Generally, the specific capacitance values of carbon-based materials are in the range of 50–350 F/g. Specific capacitance can be increased by improving the existing pore size and surface area through physical and chemical activation of carbon source materials [13].

Table 1 shows previously published related studies focusing on the high surface area ACFs and their capacitive performance. It can be clearly seen that the activation agent, activation temperature, and the carbon source are the main parameters that affect the surface area as well as the capacitive performance. However, no correlation was observed between these parameters and the specific capacitance. It is believed that the accessible and proper pore size distribution and suitable surface morphology allow faster ion transfer, hence even more effective than the surface area in some cases. As can be seen from Table 1, KOH and H_3PO_4 are widely used as activation agents [14, 15], for different types of biomass. KOH is efficacious in creating micropores, small mesopores, and, therefore, very high specific Brunauer–Emmett–Teller (BET) surface area of above 2000 m^2/g [16]. However, it requires high activation temperature and resulted in low carbon yield which can be assessed as a problem for large-scale applications. On the other hand, H_3PO_4 activation can be operated at low temperatures of 400–600 °C and led to the formation of a higher amount of mesopores [17]. H_3PO_4 not only promotes bond cleavage reactions but also facilitates crosslinking via cyclization, condensation, and forming a layer of linkage such as phosphate and polyphosphate esters which could protect the internal pore structure and thus prevent excessive burn-off in carbon activation [18]. Due to these advantages, H_3PO_4 is selected as the activation agent in our work.

In the literature, it is seen that many EDLC studies have been carried out based on both natural products and sugar derivatives. It is not possible to fully compare these studies due to the differences they contain, and the variety of parameters presented. Nevertheless, the literature comparison summarized in Table 1 will be useful in terms of evaluating the results obtained in this study. When the studies are evaluated in terms of surface area, it is seen that the general average is around 1400 m2/g, except for the extreme values [19–21]. The specific surface area of 1502 m2/g obtained in our study coincides with this trend. In the studies performed considering the Current Density, a high specific capacitance (265 F/g) value was obtained at 0.25 A/g current density. Table 1 shows that the highest value obtained for this parameter is 264 F/g [22]. In addition, in our study, a specific capacitance value of 305 F/g was obtained for a current density of 0.1 A/g. The highest and lowest values obtained according to Table 1 at 0.5 A/g current density are 365.6 F/g [21] and 182 F/g [20], respectively. In our study, a reasonable value was obtained with 238 F/g for the same current density. While the highest values of 250 F/g [23] and the lowest 92 F/g [24] are obtained in Table 1 for 1 A/g current density, a high specific capacitance value of 205.4 F/g was obtained in our study. No significant correlation was observed between the specific capacitance values and the specific surface area and Vmic/Vtop pore size ratios. This confirms the thesis in the literature that supercapacitor performance is determined by the interaction of many components such as specific surface area, pore size distribution, particle size, number of functional groups, and presence of heteroatoms.

In this study, sucrose-based ACFs were prepared by the smelting mixture of $Zn(NO_3)_2.4H_2O$ and sucrose. Zinc nitrate was used as a blowing agent [35] to increase the volume of carbon material during the caramelization of sucrose. Zinc nitrate, thanks to its low melting point, creates a homogenous mixture during the caramelization process at 120 °C. When the temperature increases to 230 °C, zinc nitrate decomposes and swells the carbonized sucrose. To investigate the effect of zinc nitrate concentration and the activation temperature on the surface porosity, morphology, and chemistry, different ACFs were prepared under different conditions. The obtained ACFs were characterized by various techniques such as BET, SEM, XPS, and Raman and Elemental analysis. The electrochemical energy storage properties of the ACF-based electrodes were determined by cyclic voltammetry (CV), galvanostatic charge–discharge (GCD), and electrochemical impedance spectroscopy (EIS).

Table 1 Literature review related to the carbon-based foams and their electrochemical performance

Carbon-based foam (synthesis and properties)							Electrochemical Performance			
Source	Foaming agent	Activation agent	Temp—Time—Heating rate	S_{BET} (m^2/g)	V_{mic} /V_{total}	V_{mes}/V_{mic}	Technique	Cur. Density / Scan Rate	Specific Cap. (F/g)	Ref.
Commercial Melamine Sponge	–	–	800 °C–3 h-5 °C/min	1136			GCD	1 A/g	92	[24]
Glucose and human hair	–	KOH	600 °C–3 h	849	0.92	0.167	GCD	0.25 A/g	264	[22]
Bamboo cellulose fibers	–	NaOH/Urea	800 °C–2 h 5 °C/min	1128	0.67	0.33	GCD	0.3 A/g	280	[25]
Shaddock peel	–	K_2CO_3	900 °C–2 h-3 °C/min	1438	–	–	GCD	0.25 A/g	225	[26]
Peanut shells		KOH	800 °C-1 h–5 °C/min	702	–	–	GCD	0.25 A/g	247	[9]
Graphite oxide-hydrogel	–	–	Hydrothermal	2110	0.03	0.97	GCD	0.5 A/g	297	[27]
Japanese citron	–	KOH	800 °C-2 h 20 °C/min	2500	–	–	CV	1 mV/s	157	[19]
Oil palm empty fruit bunches	–	KOH	850 °C-2 h 3 °C/min	2774	0.13	0.87	GCD	0.5 A/g	182	[20]
Resol resin	–	KOH	750 °C-3 h 3 °C/min	3066	0.21	0.79	GCD	0.5 A/g	365.6	[21]
Glucose	–	ADC	800 °C-2 h–4 °C/min	624.8	–	–	GCD	1 A/g	202.7	[28]
Glucose	–	CO_2	900 °C-10 h	1540	0.978	–	GCD	1 mA/cm^{-2}	158	[29]
Sucrose	–	KOH	800 °C-1 h–5 °C/min	2823	–	–	GCD	1 A/g	218	[30]
High-fructose corn syrup	–	–	850 °C-4 h	1223	0.578	0.434	GCD	0.2 A/g	168	[31]

Table 1 (continued)

Carbon-based foam (synthesis and properties)							Electrochemical Performance			
Source	Foaming agent	Activation agent	Temp—Time—Heating rate	S_{BET} (m^2/g)	V_{mic} /V_{total}	V_{mes}/V_{mic}	Technique	Cur. Density / Scan Rate	Specific Cap. (F/g)	Ref.
Glucose (White granulated sugar)	NH_4Cl	–	1350 °C-3 h–4 °C/min	1005	–	–	GCD	1 A/g	250	[23]
Sucrose	H_2SO_4	CO_2	900 °C-4 h–10 °C/min	2102	0.77	0.29	CV	1 A/g	137	[32]
Sugar	H_2SO_4	KOH	850 °C-30 min–7 °C/min	713	0.385	–	GCD	1 A/g	242.67	[33]
Graphene, Commercial activated carbon	Mg	CO_2	1 mP–5 s-15 A	1850	–	–	GCD	0.25 A/g	117	[34]
Sucrose	Zn	H_3PO_4	600 °C-1 h–10 °C/min	1502	0.428	1.190	CV	10 mV/s	215.6	This work
Sucrose	Zn	H_3PO_4	600 °C-1 h-10 °C/min	1502	0.428	1.190	GCD	1 A/g	205.4	This work

2 Materials and methods

2.1 Materials

Zinc nitrate ($Zn(NO_3)_2.4H2O$), Phosphoric acid (H_3PO_4) (85%), and Hydrochloric acid (HCl) (36.5%) were purchased from Sigma-Aldrich. The commercial activated carbon was purchased from a local supplier and dried for 3 h at 120 °C prior to use. Deionized water was obtained by using Human Corporation Zeneer Power 1 water purification system. Carbon black (CB) (CAS Number 1333–86-4, Alfa Aesar), Poly(vinylidene fluoride) (PVDF) (CAS Number 24937–79-9, MTI), and N-Methyl-2-Pyrrolidone (NMP) (CAS Number 872–50-4, Merck) were used without purification for the preparation of electrode slurry.

The Scanning Electron Microscopy (SEM) images were obtained using a JEOL 6510. Surface area and porous structure were studied by BET analyzer (Quantachrome Autosorb IQ2, USA) via nitrogen adsorption–desorption isotherms at 77 K. The degassing of samples was performed under a vacuum at 105 °C for 15 h before measurements. The surface area, total pore volume, and pore size distribution of ACFs were calculated by Brunauer–Emmett–Teller (BET) method, the Quenched Solid Density Functional Theory (QS-DFT), and Barrett-Joyner-Halenda (BJH) method. C, H, N, O, and S contents of the samples were measured by LECO / Truespec Micro NCS analyzer. XPS data were recorded by Specs-Flex XPS instrument, and Raman spectra were recorded by WITech alpha 300R at 532 nm. Gamry Interface 1010E Potentiostat/Galvanostat/ZRA was used for the electrochemical tests.

2.2 Preparation of activated porous carbon foams

The amount of sugar was kept constant and the concentration of $Zn(NO_3)_2.4H_2O$ were mixed to be 2.5, 5, 10, 20, and 50% ($Zn(NO_3)_2.4H_2O$: Sugar, wt:wt), respectively. Then the mixtures were dissolved in 6 mL of water. The mixtures were first heated in a muffle furnace at 120 °C until became viscous and then at 230 °C until the foaming was completed. The samples were named CF-X (CF: Carbon foam, X: the concentration of $Zn(NO_3)_2.4H_2O$). For example, CF-2.5 means that the %2.5 concentration of $Zn(NO_3)_2.4H_2O$ was mixed with sugar.

The resulting carbon foams (CF-X) were boiled with 0.1 M 20 mL HCl for 30 min. Then it was filtered and washed with hot distilled water until pH reached at 7 and dried in an oven at 100 °C overnight. The dried samples were impregnated with H_3PO_4 (85%) at a ratio of 4:1 (H_3PO_4/CF, wt/wt) at 85 °C in a magnetic stirrer until completely absorbed and in an oven at 100 °C for 24 h. The dried materials were carbonized in a horizontal tube furnace for an hour at 600 °C under N_2 flow of 100 mL/min with a heating rate of 10 °C/min. The carbonized samples were washed with hot distilled water until phosphoric acid was removed from the samples and it was checked by the Phosphate test whether the phosphoric acid was completely removed. Then dried in an oven at 100 °C overnight. The same processes were produced at the carbonization temperature of 700, 800, and 900 °C. The samples were named CF-XY (X: the concentration of $Zn(NO_3)_2.4H_2O$, Y: the first digit of the carbonization temperature).

2.3 Electrochemical study

As-synthesized ACFs were used as electrode active material and an electrode was composed of ACF, carbon black (CB), and poly(vinylidene fluoride) (PVDF) at a ratio of 85:05:10 by weight. All were mixed in N-Methyl-2-Pyrrolidone (NMP) for 24 h on a magnetic stirrer to ensure a homogeneous electrode slurry. The resulted electrode slurry was cast on the Pt working electrode by a simple drop-casting method. An air gun was carefully used to dry the electrode on the Pt surface. A conventional three-electrode cell was used for the electrochemical tests. Pt as working electrode, Pt plate as counter electrode, and Ag/AgCl as reference electrode were used. Cyclic voltammetry (CV), galvanostatic charge–discharge (GCD), and electrochemical impedance spectroscopy (EIS) techniques were used to determine the electrochemical energy storage characteristics. Na_2SO_4 was selected as a neutral electrolyte to avoid the change in electrode surface at different pHs. The specific capacitance of the prepared electrodes was calculated from CV and GCD according to Eq. 1 and 2, respectively [36].

$$C(F/g) = \frac{1}{mv\Delta V}\int_{V1}^{V2} i(V)dV \tag{1}$$

$$C(F/g) = \frac{I\Delta t}{m\Delta V} \tag{2}$$

where m is the mass of the full electrode, ν is the scan rate, ΔV is the working potential window (V2-V1) in the Eq. 1. In the Eq. 2, I is the applied constant current, m is the mass of the full electrode, t is time and V is the voltage.

3 Results and discussion

3.1 Characterization of bare and activated porous carbon foams

In the first stage, sucrose was used as a carbon source in the production of carbon foam. Sucrose, a hydrocarbon, is a

suitable material for the preparation of meso/macroporous carbons with microporosity in the inner parts of the carbon walls because it increases microporosity in carbon foam formation [37]. $Zn(NO_3)_2.4H_2O$ was used as the foaming agent. When zinc nitrate is heated with sucrose above its melting point, it provides the formation of porous carbon foams without the need for additional gases. The basic mechanism of obtaining carbon foam from sucrose with $Zn(NO_3)_2.4H_2O$ can be considered as the swelling of sucrose, which is caramelized, with nitrogen oxides and water vapor formed during the decomposition of zinc nitrate (Fig. 1). In this way, micro and mesopores occur in the structures of the carbon foams formed by the removal of these gases.

In addition, to remove the remaining Zn compounds and the inorganic impurities in the sample, it was washed with a low concentration acid solution (HCl). The obtained samples are impregnated with H_3PO_4 solution as a chemical activation agent without the need for an additional purification process and subsequently, hierarchically porous carbon materials are formed by carbonizing in an inert environment. Improved surface area, pore-volume, and pore diameter properties of activated carbons used in the electrochemical double-layer capacitor (EDLC) applications are the determining parameters of their electrochemical properties. Activated carbon samples prepared by considering these parameters is possible to increase the specific capacitance value.

3.2 Effect of Zn concentration and activation temperature on the surface characteristics

To investigate the effect of $Zn(NO_3)_2$ concentration on the surface area of the carbon foam, the activated carbons were prepared from different $Zn(NO_3)_2$ concentrations, keeping other parameters constant. N_2 adsorption–desorption isotherms of the samples CF-2.5–6; CF-20–6 and CF-20–7 can be seen in Fig. 2.

The BET surface areas of these samples were calculated as 1127 m^2/g, 1502 m^2/g, and 1668 m^2/g, respectively. As

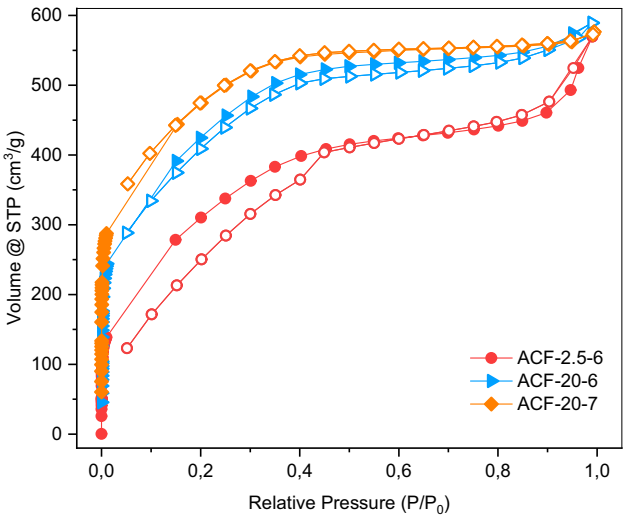

Fig. 2 N_2 adsorption/desorption isotherms of ACFs

can be understood from the N_2 adsorption/desorption isotherms, the microporosity of the samples increased with the increasing concentration of $Zn(NO_3)_2.4H_2O$.

In general, Type I isotherms, typical for microporous adsorbents, were observed in all samples. Although all samples have a microporous structure, except for the CF-20–7 sample, they also preserved the Type IV isotherms indicating the mesoporous structure. The H4 Hysteresis loops in Type IV isotherms are due to the formation of mesoporous. The hysteresis seen in the CF-2.5–6 and CF-20–6 isotherms indicates that the mesoporosity of the sample is more than those of other samples. The removal of Zn species, which is formed in the carbon foaming process, and then the use of H_3PO_4 as an activating agent led to the formation of mesopores in the structure of the final product. The total volume of micropores and mesopores indicates that the samples have heterogeneous pore distribution (Table 2). It is seen in Table 2 that the micropore volume of ACFs increases by increasing the concentration of $Zn(NO_3)_2$. Therefore,

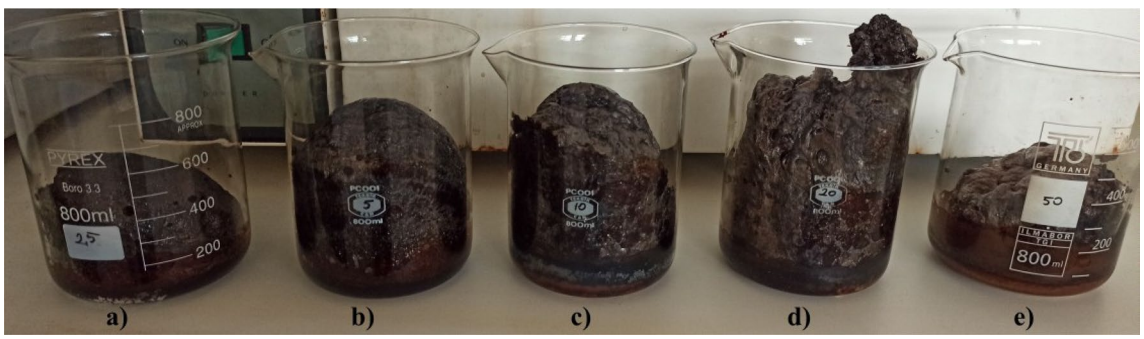

Fig. 1 Carbon foams obtained from sucrose with different concentrations of $Zn(NO_3)_2$, respectively. **a** CF-2.5, **b** CF-5, **c** CF-10, **d** CF-20, **e** CF-50

Table 2 Effects of Zn concentration and activation temperature on the surface area and pore distribution of ACFs

Sample	SBET (m2g−1)	Vmicro a (cm3 g−1)	Vmeso b (cm3 g−1)	Vtotal pore c (cm3 g−1)	% Vmicro	% Vmeso	Vmes/ Vmic	Pore Dia. (4 V/A) (nm)
CF-20–6-foam[d]	4	–	–	–	–	–	–	–
CF-20–6-HCl[e]	81	–	–	–	–	–	–	–
CF-2.5–6	1127	0.279	0.462	0.812	35	57	1.66	2.881
CF-5–6	1273	0.262	0.524	0.854	31	61	2	2.683
CF-10–6	1700	0.460	0.430	0.974	47	44	0.93	2.291
CF-20–6	1502	0.378	0.453	0.884	43	51	1.19	2.354
CF-50–6	1483	0.247	0.854	1.168	41	58	1.41	3.151
CF-20–7	1668	0.457	0.356	0.892	51	40	0.78	2.138
CF-20–8	1974	0.519	0.453	1.062	49	43	0.87	2.152
CF-20–9	1797	0.398	0.649	1.137	35	57	1.63	2.532

[a]V_{micro} at 2 nm (QSDFT)

[b]$V_{meso} > 2$ nm (QSDFT)

[c]$V_{total\ pore}$ at $P/P_0 \approx 0.99$

[d]only carbon foam, [e]without H_3PO_4 chemical activation

changes in the surface area also have a linear relationship with the increasing Zn concentration. Sucrose has been carbonized without being activated with zinc nitrate, and its surface area is calculated as 247 m^2/g [38]. In the present study, thanks to the H_3PO_4 activation of carbon foam samples higher specific surface area has been obtained.

The activation temperature has significantly changed the total pore volume, bond structures, and the amount of surface functional groups. The change in the activation temperature affecting the surface area and the electrical conductivity of the ACFs are two critical factors that determined the values of their use in many technological applications. However, in electrode materials, it is not possible to evaluate the surface area independently of the pore volumes [39]. Therefore, the effect of activation temperature on the structure of ACFs was investigated in this study. We aimed to improve the electrical conductivity properties of activated carbon foams by chemical activating the samples at higher temperatures while keeping the surface area relatively high.

To investigate the effect of the activation temperature on the specific surface area, different activation temperatures (600, 700, 800, 900 °C) were studied for the CF-20 sample, which showed the best electrochemical properties among the synthesized ACFs prepared by different concentrations of zinc nitrate. As can be seen in Table 2, the specific surface areas of the samples (1502 m^2/g, 1668 m^2/g, 1974 m^2/g, respectively) were increased with temperature except for 900 °C (1797 m^2/g). The probable cause of this situation may be the transformation of micropores to mesopores at 900 °C. At the activation temperature, the H_3PO_4 acts as an acid catalyst supporting bond cleavage and crosslinks formation. However, when the temperature increased to 900 °C, because of the coalescence of adjacent pores at an extreme burn-off or the enlargement of the existing small pores specific surface area was decreased [40].

The effect of activation temperature on the porosity of the synthesized ACFs activated at high temperatures on the pore size distributions is determined by the QSDFT method (Table 2). According to Fig. 3, the increase in the amount of $Zn(NO_3)_2$ has no significant effect on the total pore volume. For the samples CF-2.5, CF-5, and CF-10, an increase in the zinc nitrate concentration supported micropore formation, while a decrease in the micropore volume was observed at higher concentrations. On the other hand, there was no significant change in the mesopore volume with the increased zinc nitrate concentration, except for the sample CF-50.

While the activation temperature increased from 600 °C to 700 °C, the micropore volume increased, while the mesoporous volume decreased. It was seen that these results were consistent with pore size distributions (Figure S1). Micropore and mesopore volumes of the samples increased while the activation temperature reached 800 °C. When the activation temperature reached 900 °C, the mesopore volumes increased considerably and the micropore volumes decreased. In addition, it was understood from the significant decrease in activated carbon yield that the carbon compounds burn off under the influence of high temperatures. Probably, increasing temperature caused mesopores to be formed by the coalescence of micropores. Moreover, this change in pore size distribution led to a decrease in the surface area of the ACFs [41].

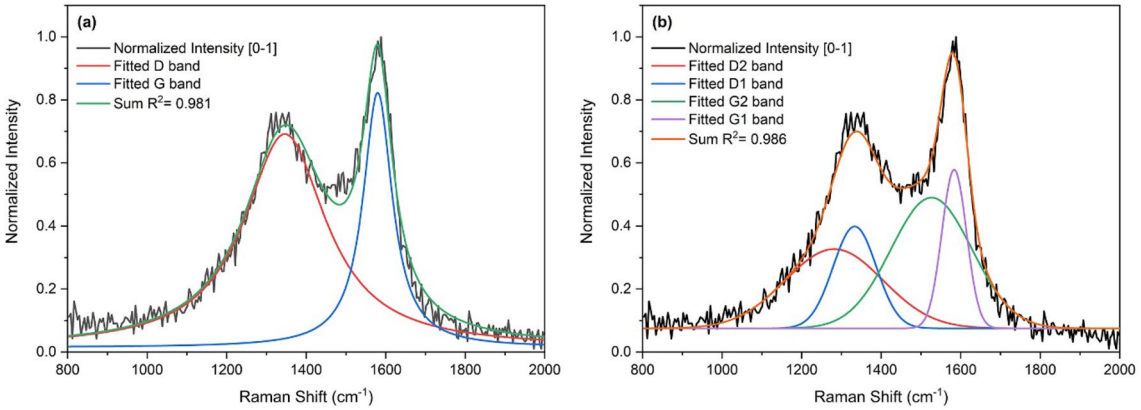

Fig. 3 Deconvolution of Raman spectra into **a** 2 peaks **b** 4 four peaks of the Sample CF-20–6

3.3 Effect of activation temperature on the elemental composition

The elemental analysis results of ACFs prepared at different temperatures were shown in Table S1. As can be seen, the carbon and oxygen contents of the samples, while increasing temperature, the percentage of carbon increased, and oxygen contents decreased. These results clearly showed that oxygenated moieties, having low thermal stability, were released from the structure.

3.4 SEM—Effect of Zn concentration and activation temperature on the surface morphology

Scanning electron microscopy (SEM) images of activated carbons show a sponge-like morphology with heterogeneous pores (Figure S2). With increasing the amount of $Zn(NO_3)_2$, it was seen that the activated carbons became more porous, and smaller pores were formed. The formation of porosity starts with the decomposition of sucrose and zinc nitrate in the carbon foams. Micro/meso and macropores may occur due to the removal of various gases such as NO_x, N_2, CO_2, etc. from the structure. But main porosity formation occurs during chemical activation. The present study shows that the existing pores in the morphology of the samples changed depending on the H_3PO_4:carbon foam ratio (4:1) (Figure S2a-e (left)). Although some micropores remained intact, some large-sized pieces with sharp edges were formed by the chemical activation of H_3PO_4 (Figure S2b,c). H_3PO_4 contributes to the further development of mesoporous due to the decomposition of phosphocarbon species and the formation of volatile phosphorus-containing compounds (P_4, P_4O_{10}, etc.) because of redox reactions occurring between various phosphate compounds and carbon with the activation process (Figure S2) [42]. The porous structure of ACFs plays an important role in the diffusion of electrolyte ions into the interior of the electrode [43]. Hierarchical porous materials with appropriate pore size distribution and large surface area show excellent electrochemical performance. The ion transport distance is shorter in mesopores and a large surface area is the ability to store a large amount of charge, resulting in high capacitance performance is ensured.

The structural morphology of ACFs obtained at different activation temperatures was investigated by SEM (Scanning electron microscope) (Figure S2d,f,g). SEM images are considered together with the N_2 adsorption isotherms, the micro and mesopores dispersed below 10 nm in the activated carbons only appear as a rough surface in the SEM images. Although SEM images do not give any significant information on the distribution of porosity, the increase in surface roughness due to the increasing temperature at 10 k magnification coincides with the trend of increasing mesoporosity with temperature obtained from the N_2 adsorption results.

The morphological structure of the ACFs obtained from sucrose is non-uniform and irregular. One of the most important factors affecting the surface area and pore structure of ACFs is activation temperature. In this process, active pores are formed on the surface. The effect of thermal treatment on ACF can be evaluated in Figure S2d. As the carbonization temperature was increased from 600 °C to 700 °C, it affected the morphology of the material with an average pore diameter of 2.35 nm, increasing the microporosity and decreasing the mesoporosity. Thus, the average pore diameter decreased to 2.14 nm. (Figure S2f). On the other hand, it was observed that there was no significant change in the average pore diameter and porosity with the increase of the carbonization temperature to 800 °C (Figure S2g).

3.5 Raman analysis

Raman spectroscopy has become a key technique for the characterization of sp^2 hybridized carbon materials such as activated carbons, graphene, and carbon nanotubes due to its sensitivity to changes in the structure of carbons. Figure 3 shows the deconvolution of the partial Raman spectra of the Sample CF-20–6 into two and four Lorentzian peaks in order to discuss the changes in the chemical structure of ACFs in detail. Two characteristic peaks were observed for all samples (now shown here); the first peak in the 1300–1400 cm^{-1} ranges, is attributed to the disorder-induced band of graphitic carbon (D band), and the second peak at around 1500–1600 cm^{-1} ranges corresponds to in-plane vibrations of graphitic structure (G band) [44]. The G and D bands exhibit an overlap without a clear separation, which is typical for disordered activated carbons [45]. First, the normalized experimental curves were deconvoluted to G and D bands by using two Lorentzian peaks to determine the ratio of 'disordered part' to 'ordered part'. The calculated I_D/I_G ratios from two peak deconvolution, and I_{D1}/I_{G1} and I_{D2}/I_{G2} ratios from four peak deconvolution are presented in Table S2. Due to the I_D/I ratios, no significant differences were observed between the samples except CF-5–6. The presence of more 'ordered parts' in Sample CF-5–6 does not make any sense and cannot be able to explain with currently available data. In the four peak deconvolution, the similar and sharper peaks, G1 and D1 are assigned to the winding short basal plane of graphite with bond angle order, while the broader G2 and D2 peaks are associated with the amorphous sp^2 carbon clusters with bond disorder [45]. Higher I_{D1}/I_{G1} and lower I_{D2}/I_{G2} ratios of the samples CF-10–6 and CF-20–8 than those in other samples indicate reduced sizes of both basal planes and amorphous carbon clusters [46]. The lower I_{D1}/I_{G1} ratio and higher of I_{D2}/I_{G2} ratio in the samples CF-20–6 and CF-50–6 corresponds to the formation of larger basal planes with fewer defects and larger amorphous carbon domains from possibly two opposing effects on carbon microstructures, respectively [46]. Smaller basal planes and much more surface defects may lead to low capacitive performance due to the formation of ruptures on the electron conduction pathways. It is thought that these complicated results originated from the uncontrollable and probable formation of radical species and gaseous products during the foaming process. The partially graphitic porous structure with developed hierarchical pores with fewer defects and well connectivity is expected to improve the electrochemical behaviors of ACFs [47].

3.6 XPS analysis

The presence and the amount of surface functional groups (SFGs) which contribute to the total specific capacitance by creating pseudocapacitance and increasing the wettability of the electrode were evaluated by XPS analysis. Figure 4 shows the deconvolution of C1s spectra of the Sample CF-20–6 and the calculated amounts of SFGs for all samples by considering the total carbon content in the sample. As a result of the presence of several SFGs on the carbon surface, complicated envelopes were observed in C1s spectra for all samples. Main characteristic peaks at around 284.5 eV, 285.8 eV, 286.6 eV, 287.4 eV, and 288.9 eV assigned to graphitic carbon or sp^2 carbon (C = C); C atoms directly bonded to O in hydroxyl configurations (C – O in phenol or alcohol); epoxide groups (C–O–C); carbonyl groups (> C = O), and carboxyl groups (COOH or HO-C = C), respectively. The assignments are in good agreement with previously reported data. No peak was observed at around 290.5–290.9 eV corresponding to π-π^* transition due to the bond breakage at the edge of

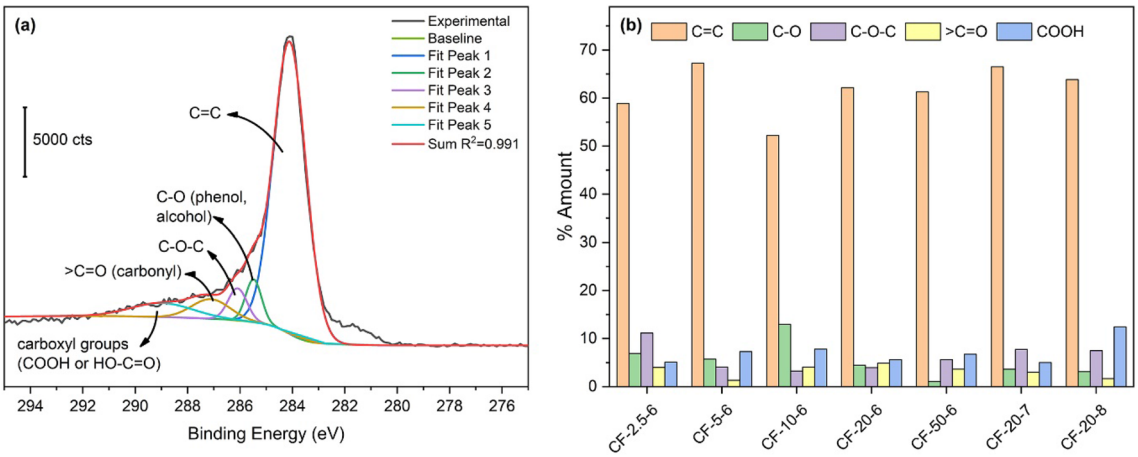

Fig. 4 **a** Deconvolution of C1s spectra of the Sample CF-20–6, and **b** the amounts of SFGs obtained by the deconvolution of C1s spectra of the samples

the planar structure during the calcination process [48]. The formation of the above SFGs can be explained by these chemically active radicals to heteroatoms (O and H) to form surface complexes or functional groups [48, 49]. There is no correlation found between the Zn concentration and the amount of the above SFGs. This can be attributed to the uncontrollable formation of radical species and gaseous products during the foaming process. However, the activation temperature significantly affected the amount of SFGs. The number of phenolic/alcohol groups and carbonyl groups decreased while the ether and carboxylic groups increased with the increasing activation temperature. In the case of sp^2 hybridized carbon (C = C), first an increase and then a decrease was observed. Among these SFGs, carbonyl groups are believed to be electrochemically inactive; however, the carboxyls/carbonates, quinone, and hydroxyls [50] [50] are expected to create pseudo-capacitance due to the kinetics of the redox reactions [51]. In addition, all these SFGs also enhance the wetting of electrode surface by electrolyte [52]. Therefore,

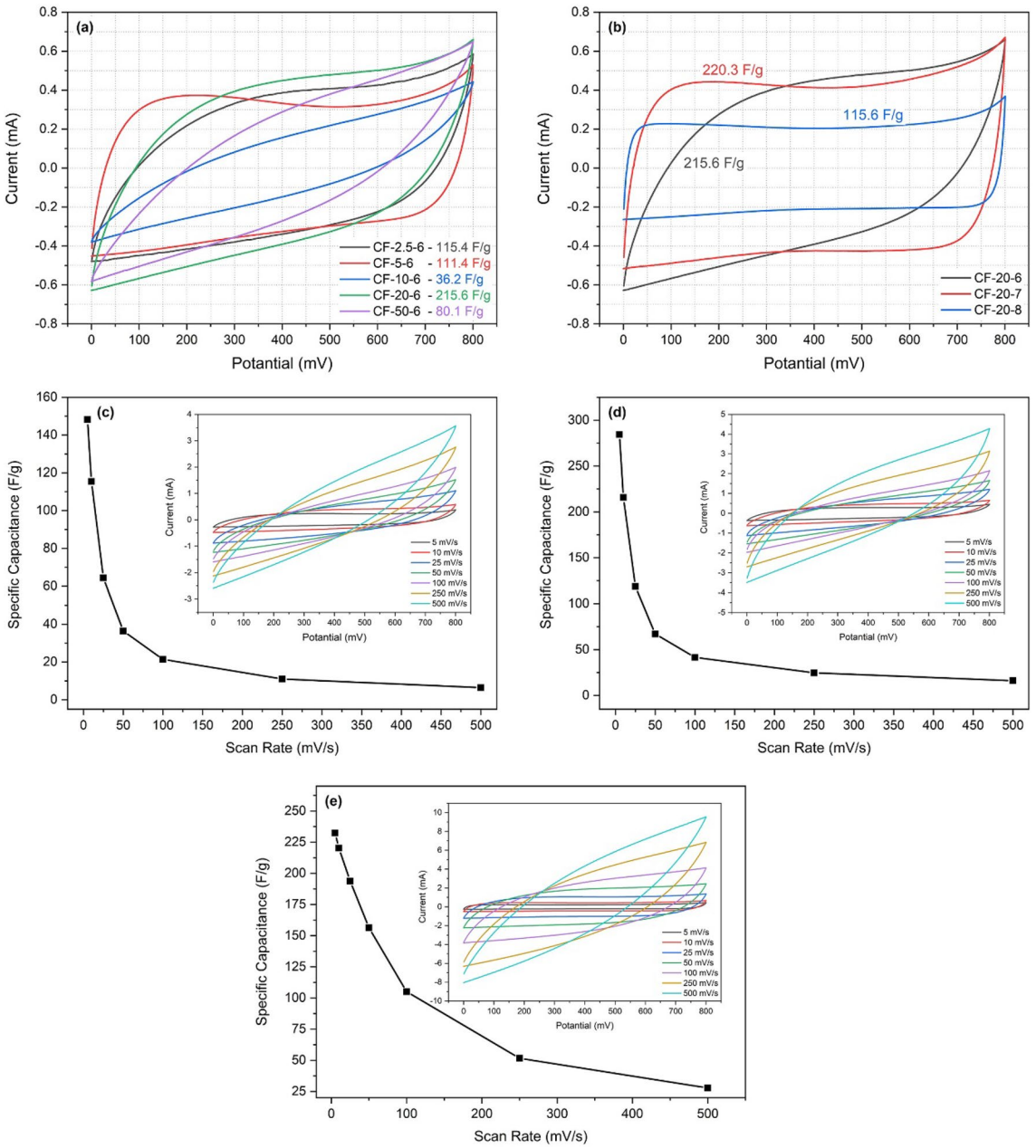

Fig. 5 The CV curves of the ACFs synthesized **a** at different concentrations of Zn, **b** at different activation temperatures at the scan rate of 10 mV/s, the change in the calculated specific capacitance vs. scan rate **c** CF-2,5–6, **d** CF-20–6 and **e** CF-20–7 (inset graphics are CV curves)

the sample CF-20–6 is expected to present higher capacitive performance compared to others due to the high content of phenolic/alcohol and carbonyl groups.

3.7 Electrochemical properties of ACF-based electrodes

The effects of Zn concentration and activation temperature on electrochemical characteristics and charge storage performances were investigated using CV, GCD, and EIS in a conventional 3-electrode cell configuration. Figure 5a and b show the CV curves of the synthesized ACFs with different Zn concentrations and activation temperatures at a scan rate of 10 mV/s, respectively. All samples except CF-10–6 and CF-50–6 exhibit roughly rectangular shapes indicating typical double-layer capacitance characteristics [53]. The distortions observed between 50 and 400 mV might be attributed to the reversible redox reactions originating from the SFGs on the activated carbon [54, 55]. According to the specific capacitance calculated from the CV curves, no correlation was found between the changing Zn concentration and specific capacitance. Although the Sample CF-10–6 had a high surface (1700 m^2/g) area and micropore volume (0.460 cm^3/g), it showed the lowest capacitive performance. The higher mesopore volume than micropore volume may be one of the reasons. As a result of the high mesopore volume, the mobility of the electrolyte ions gets faster, consequently, the ability of the energy storage of the micropores slows down. In addition, the increased wettability of the surface of CF-10–6 due to the high number of carbonyl groups supports this idea. Moreover, the reduced sizes of both basal planes and amorphous carbon clusters, and the lower sp^2 carbon content may contribute to decreasing the capacitive performance. In Fig. 5b, it can be seen that the increase in the activation temperature led to changes in the shape of the CV curves to a more rectangular form. However, the calculated specific capacitance decreased dramatically. The effect of SFGs on the CV curves disappeared when the temperature increased from 600 °C to 800 °C as a result of the breaking of oxygen-containing SFGs with the temperature and release as gaseous products.

The change of the calculated specific capacitance with the scan rate and the CV curves (inset) can be seen in Fig. 5c, d, and e. As expected, a drastic decrease in the calculated specific capacitance was observed for all samples while the scan rate ranges from 5 mV/s to 50 mV/s. The trend in

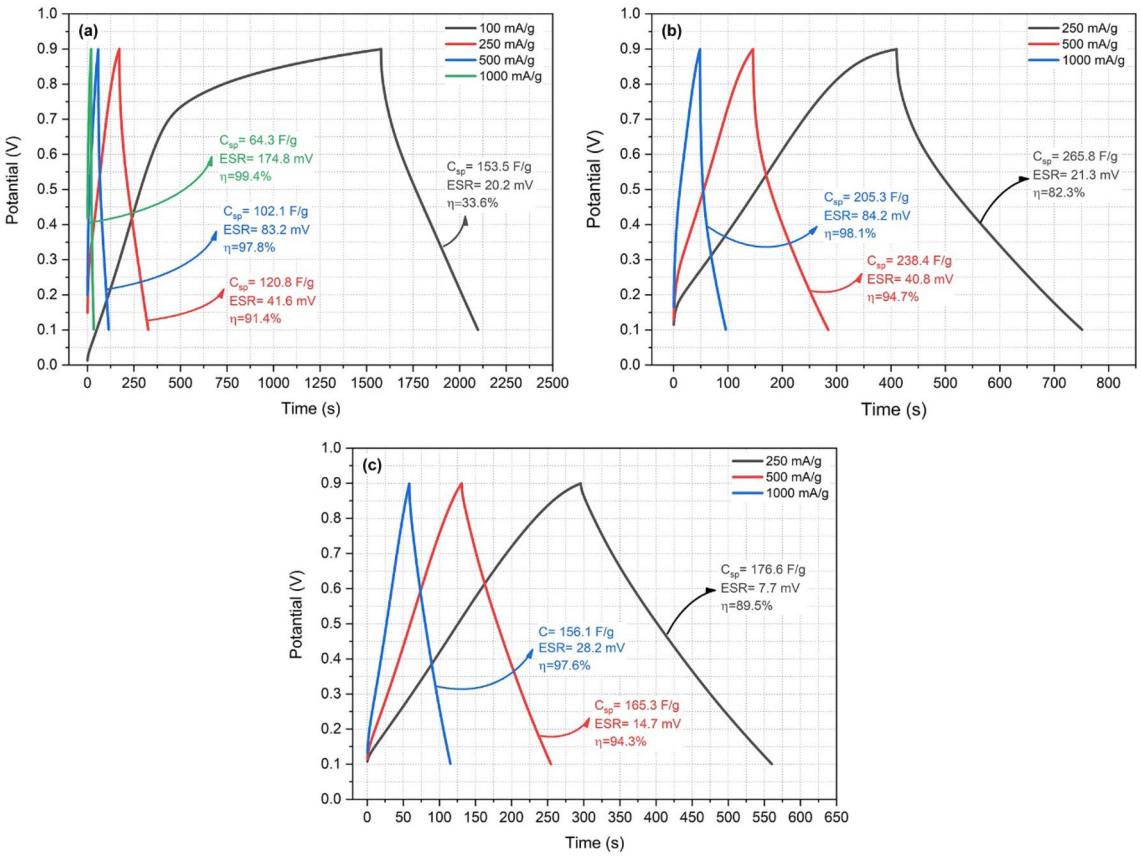

Fig. 6 GCD curves of the samples **a** CF-2.5–6 **b** CF-20–6 and **c** CF-20–7 at different current densities

the decrease continued with a slower rate from 50 mV/s to 500 mV/s. Since the calculated specific values calculated from CV and GCD analysis are quite different [56]. We find to use GCD data over CV data is more accurate.

Figure 6 represents the GCD curves of the samples CF-2,5–6, CF-20–6, and CF-20–7 at different current densities ranging from 100 mA/g to 1000 mA/g. The symmetrical triangular shape of the GCD curves suggests the formation of electrochemical double layers at the electrode/electrolyte interface [57]. As shown in Fig. 6a, the GCD curves do not display a perfect triangular shape at the 100 mA/g current density due to the inadequate current to charge the electrode. Therefore, the results obtained at 100 mA/g were disregarded and not shown for other samples due to the low Coulombic efficiency. For the sample CF-2,5–6, the specific capacitance decreased nearly 50% with the increasing current density from 500 mA/g to 1000 mA/g indicating the low rate capability. However, the samples CF-20–6 and CF-20–7 showed higher rate capabilities. The ESR values increased with the increasing current density, as expected, due to the increase in the mobility of charge. The higher ESR values also caused a disruption in the triangular shape of GCD curves, as can be seen for the CF-20–6 sample. As a result, low ESR values, high specific capacitance, and high Coulombic efficiency prove that the synthesized ACFs are good candidates for EDLC applications.

The specific capacitance and ESR values for all samples are given in Table 3 to discuss the relationship between the specific capacitance, Zn concentration, and activation temperature. As can easily be seen, there is no correlation between the Zn concentration and the capacitive performance of ACF-based electrodes. However, an increase in the activation temperature caused lower specific capacitance and ESR. Despite the increase in surface area, the decrease in the specific capacitance shows that the surface morphology and chemistry are more effective. The ESR drop depends on the resistance between electrolyte, collector and electrode, SGFs, and pore characteristics [58]. The formation of the porous structure can be seen in SEM images. Again, the increase in the surface roughness led to the formation of pathways resulting in an increase in electrolyte mobility, and a decrease in the mass transfer resistance. As a result, the ESR drop decreased significantly with the increasing activation temperature of ACFs.

With the increase in current density, calculated specific capacitance decreases at certain rates, as expected. This can be explained by the following: *i)* decreasing the contact time of electrolyte and electrode with the increased scan rate or current density resulting in less charge storage [59, 60]; *ii)* Contribution of ESR drop and slowing kinetics of electrochemical activities at high current densities, and *iii)* decrease in the thickness of the electrochemical double layer due to the increase in the electrolyte mobility. A lower decrease in the specific capacitance with the increasing current density is expected for the rate capability. For our samples, again no correlation was observed between the Zn concentration and the rate capability. However, the activation temperature led to an increase in the rate capability of the ACF-based electrodes.

Figure 7 shows the EIS data of the selected samples in a three-electrode cell configuration. Three distinct regions in Nyquist plots, the intercept at the real axis, a semicircle in the high-frequency region, and a linear part over low frequency give information about intrinsic resistance of electrode materials, ionic resistance of the electrolyte, electrode conductivity, and the charge-transfer resistance [61]. In the low-frequency region, the closer the slope of the straight line (perpendicular to the x-axis) is to 90°, the closer to the ideal capacitive behavior. The slope values read from the Bode plots (not shown here) can be seen in Fig. 7a. All samples are very close to the ideal capacitor except the sample CF-2,5–6. In the intermediate frequency region, the Warburg line (45°slope) and following nearly straight vertical line were observed for all samples indicating that all samples possess ideal capacitor behavior and allow the electrolyte ions to be adsorbed on the electrode surface [62]. Moreover, the slower ion diffusion leads to the longer Warburg line [37]. Therefore, it is obvious that the increase in the activation temperature led to the higher electrical conductivity of electrodes. In the high-frequency region (Fig. 7b), the diameter of the semicircle got larger with the increasing activation temperature implying the increasing charge transfer resistance. It can easily be said that the

Table 3 Calculated specific capacitance and ESR values from GCD curves for all samples at different current densities (C_{sp} is F/g and ESR is mV)

Sample	100 mA/g		250 mA/g		500 mA/g		1000 mA/g	
	Csp	ESR	Csp	ESR	Csp	ESR	Csp	ESR
CF-2.5–6	153.5	20.2	120.9	41.6	102.1	83.2	64.3	174.8
CF-5–6	101.9	8.4	88.7	17.2	83.1	32.9	70.1	66.2
CF-10–6	209.3	71.7	172.4	154.9	14.1	296.5	< 10	> 400
CF-20–6	305.1	9.8	265.8	21.3	238.4	40.8	205.4	84.2
CF-50–6	252.1	34.3	194.3	77.7	170.6	171.7	18.2	310.8
CF-20–7	207.5	4	176.6	7.7	165.3	14.7	156.1	28.2
CF-20–8	103.9	3.3	91.1	6.5	86.9	12.3	83.7	22.4

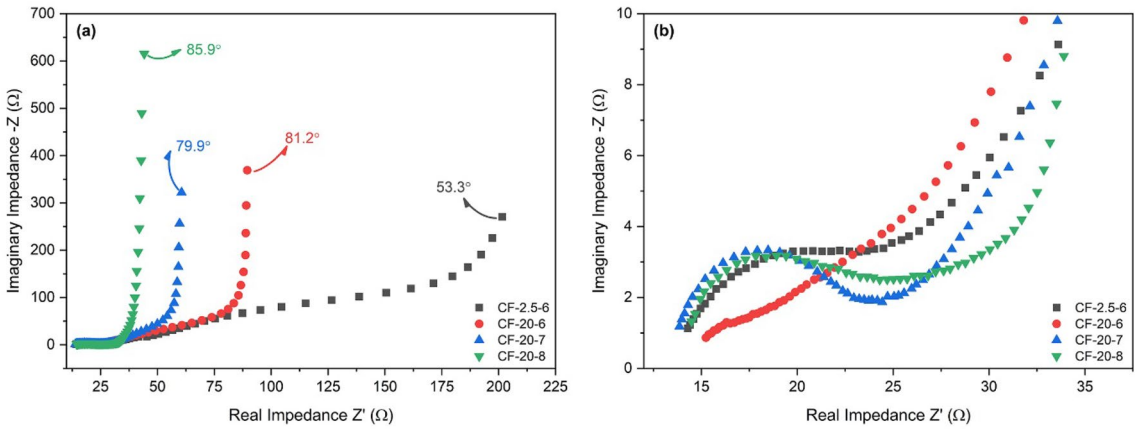

Fig. 7 Effect of Zn concentration and activation temperature on the electrochemical impedance, Nyquist plots **a** All frequency regions, **b** High-frequency region

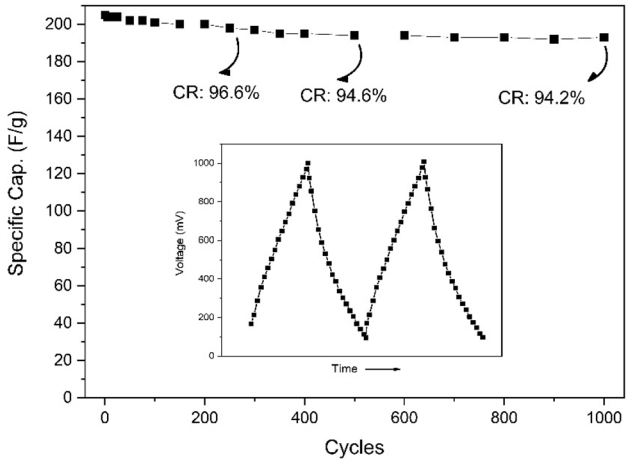

Fig. 8 Cycling stability of CF-20–6 sample

CF-20–6 sample has the lowest charge transfer resistance and the highest electric conductivity in the high-frequency region.

The cycling stability of the CF-20–6 sample at a current density of 1A/g over 1000 cycles with the charge–discharge curves for the 999th and 1000th cycles can be seen in Fig. 8. The specific capacitance of the electrode decreased from 205 F/g to 193 F/g during 1000 cycles. The capacitive retention is calculated as 96.6%, 94.6% and 94.2% after 250, 500 and 1000 cycles, respectively. It is obvious that the electrode is highly stable and shows high cycling performance and electrochemical reproducibility.

4 Conclusion

In summary, activated carbon foams were synthesized, and characterized by various techniques. The effect of Zn concentration and activation temperature on the surface area, pore size distribution, and surface morphology were discussed as well as electrochemical energy storage characteristics. No correlation was found between the Zn concentration and electrochemical characteristics; however, the activation temperature had a determinative effect on the surface, chemical, and electrochemical properties. These ACFs exhibited a specific capacitance of 265.8 F/g at a current density of 250 mA/g. The specific capacitance decreased to 205.4 F/g while the current density increased to 1000 mA/g. The high charge storage capacity can be attributed to double-layer formation led by complex micro/mesoporosity with high surface area, and the Faradaic effect originated from oxygen-containing surface functional groups. Moreover, it is found that surface morphology plays a key role since the double layer formation is strongly dependent on the surface.

Supplementary Information The online version contains supplementary material available at https://doi.org/10.1007/s10934-022-01372-5.

Acknowledgements This study was supported by Recep Tayyip Erdogan University—Research Funding—(FBA-2020-1146).

Author contribution Z.Ö and M.A.Ö did the experiments, prepared the figures, and wrote the original draft. H.T.A and T.Y determined the concept of the work and edited the final version of the paper. H.T.A. was the project coordinator for financial support. T.Y was the supervisor of the study. All authors reviewed and accepted the uploaded version of the manuscript.

Declarations

Competing interests The authors declare that they have no known competing financial interests or personal relationships that could have appeared to influence the work reported in this paper.

References

1. S.L. Liu, Y.N. Wang, K.T. Lu, J. Porous Mater. **21**, 459 (2014)
2. N. C. Gallego and J. W. Klett, in *Carbon N Y* (2003), pp. 1461–1466.
3. P. Jana, V. Ganesan, Carbon N Y **47**, 3001 (2009)
4. H. Parsimehr, A. Ehsani, S.G. Moghadam, W.A.D.M. Jayathilaka, S. Ramakrishna, Chem. Record **21**, 1098 (2021)
5. A. Ehsani, H. Parsimehr, Adv. Colloid. Interface. Sci. **284**, 102263 (2020)
6. A.A. Kudinova, M.E. Poltoratckaya, R.R. Gabdulkhakov, T.E. Litvinova, V.A. Rudko, J. Porous Mater. **29**, 1599 (2022)
7. M.B. Kabataş, S. Çetinkaya, J. Porous Mater. **29**, 1211 (2022)
8. United States Department of Agriculture Foreign Agricultural Service, *Sugar: World Markets and Trade* (2022).
9. T. Manimekala, R. Sivasubramanian, S. Karthikeyan, and G. Dharmalingam, Journal of Porous Materials (2022).
10. H. Mostaanzadeh, M. Shahmohammadi, A. Ehsani, M. Moharramnejad, E. Honarmand, J. Mater. Sci.: Mater. Electron. **32**, 26539 (2021)
11. M. Inagaki, H. Konno, O. Tanaike, J Power Sources **195**, 7880 (2010)
12. C. Portet, G. Yushin, Y. Gogotsi, J Electrochem Soc **155**, A531 (2008)
13. L. Zhang, X.S. Zhao, Chem Soc Rev **38**, 2520 (2009)
14. H. Parsimehr, A. Ehsani, Green Chem. **22**, 8062 (2020)
15. A. Ehsani, H. Parsimehr, Chem. Rec. **20**, 820 (2020)
16. Z. Yang, R. Gleisner, D.H. Mann, J. Xu, J. Jiang, J.Y. Zhu, Polymers (Basel) **12**, 2829 (2020)
17. P. Patnukao, P. Pavasant, Bioresour Technol. **99**, 8540 (2008)
18. J. Xu, L. Chen, H. Qu, Y. Jiao, J. Xie, G. Xing, Appl Surf Sci **320**, 674 (2014)
19. T. Tsubota, Y. Hohshi, T. Ohno, S. Kumagai, J. Porous Mater. **27**, 727 (2020)
20. H.T.T. Dieu, K. Charoensook, H.C. Tai, Y.T. Lin, Y.Y. Li, J. Porous Mater. **28**, 9 (2021)
21. T. Yan, K. Wang, X. Wang, J. Porous Mater. **28**, 1187 (2021)
22. W. Si, J. Zhou, S. Zhang, S. Li, W. Xing, S. Zhuo, Electrochim Acta **107**, 397 (2013)
23. X. Wang, Y. Zhang, C. Zhi, X. Wang, D. Tang, Y. Xu, Q. Weng, X. Jiang, M. Mitome, D. Golberg, and Y. Bando, Nat Commun (2013).
24. M. Cao, Y. Feng, R. Tian, Q. Chen, J. Chen, M. Jia, J. Yao, Carbon N Y **161**, 224 (2020)
25. X. Pang, M. Cao, J. Qin, X. Li, X. Yang, J. Porous Mater. **29**, 559 (2022)
26. S.-J. Long, C.-D. Si, J. Porous Mater. **29**, 1639 (2022)
27. H.Y. Fu, C. Lu, Y.H. Huang, J. Li, Y.J. Wu, J. Porous Mater. **27**, 11 (2020)
28. X. Huang, Q. Wang, X.Y. Chen, Z.J. Zhang, J. Electroanal. Chem. **748**, 23 (2015)
29. T. Tooming, T. Thomberg, H. Kurig, A. Jänes, E. Lust, J Power Sources **280**, 667 (2015)
30. L. Mao, Y. Zhang, Y. Hu, K.H. Ho, Q. Ke, H. Liu, Z. Hu, D. Zhao, J. Wang, RSC Adv **5**, 9307 (2015)
31. W. Cao, F. Yang, Mater Today Energy **9**, 406 (2018)
32. L. Wei, G. Yushin, Carbon N Y **49**, 4830 (2011)
33. K.O. Oyedotun, F. Barzegar, A.A. Mirghni, A.A. Khaleed, T.M. Masikhwa, N. Manyala, ACS Sustain Chem Eng **7**, 537 (2019)
34. C. Li, X. Zhang, Z. Lv, K. Wang, X. Sun, X. Chen, Y. Ma, Chem. Eng. J. **414**, 128781 (2021)
35. M.J.G. de Araújo, J. Villarroel-Rocha, V.C. de Souza, K. Sapag, S.B.C. Pergher, J. Anal. Appl. Pyrolysis. **141**, 104627 (2019)
36. T. Yumak, S. Yumak, A. Karabulut, Turk J. Chem. **45**, 1488 (2021)
37. R. Ryoo, S.H. Joo, S. Jun, J. Phys. Chem. B **103**, 7743 (1999)
38. M. Armandi, B. Bonelli, F. Geobaldo, E. Garrone, Microporous Mesoporous Mater. **132**, 414 (2010)
39. B. Liu, H. Shioyama, H. Jiang, X. Zhang, Q. Xu, Carbon N Y **48**, 456 (2010)
40. W. Xu, J. Liu, K. Sun, Y. Liu, C. Chen, A. Wang, H. Sun, BioResources **16**, 4007 (2021)
41. W.M.A.W. Daud, W.S.W. Ali, M.Z. Sulaiman, Carbon N Y **38**, 1925 (2000)
42. M. Myglovets, O.I. Poddubnaya, O. Sevastyanova, M.E. Lindström, B. Gawdzik, M. Sobiesiak, M.M. Tsyba, V.I. Sapsay, D.O. Klymchuk, A.M. Puziy, Carbon N Y **80**, 771 (2014)
43. T. Adinaveen, L.J. Kennedy, J.J. Vijaya, G. Sekaran, J. Mater. Cycles Waste Manag **17**, 736 (2015)
44. D. Mattia, M.P. Rossi, B.M. Kim, G. Korneva, H.H. Bau, Y. Gogotsi, J. Phys. Chem. B **110**, 9850 (2006)
45. N. Shimodaira, A. Masui, J Appl Phys **92**, 902 (2002)
46. S. Hu and Y.-L. Hsieh, (2017).
47. H. Wang, D. Zhang, T. Yan, X. Wen, J. Zhang, L. Shi, Q. Zhong, J. Mater. Chem. A Mater. **1**, 11778 (2013)
48. J.X. Guo, X.L. Liu, D.M. Luo, H.Q. Yin, J.J. Li, Y.H. Chu, Ind Eng. Chem. Res. **54**, 1261 (2015)
49. H.F. Gorgulho, J.P. Mesquita, F. Gonçalves, M.F.R. Pereira, J.L. Figueiredo, Carbon N Y **46**, 1544 (2008)
50. M. Kim, I. Oh, J. Kim, Electrochim Acta. **196**, 357 (2016)
51. L. Wei, G. Yushin, Nano Energy **1**, 552 (2012)
52. M.J. Bleda-Martínez, J.A. Maciá-Agulló, D. Lozano-Castelló, E. Morallón, D. Cazorla-Amorós, A. Linares-Solano, Carbon N Y **43**, 2677 (2005)
53. X. Wang, D. Kong, Y. Zhang, B. Wang, X. Li, T. Qiu, Q. Song, J. Ning, Y. Song, L. Zhi, Nanoscale **8**, 9146 (2016)
54. C. Poochai, C. Sriprachuabwong, N. Srisamrarn, Y. Chuminjak, T. Lomas, A. Wisitsoraat, A. Tuantranont, Appl. Surf. Sci. **489**, 989 (2019)
55. F. Ma, S. Ding, H. Ren, Y. Liu, RSC Adv. **9**, 2474 (2019)
56. M.D. Stoller, R.S. Ruoff, Energy. Environ. Sci. **3**, 1294 (2010)
57. A. Bello, F. Barzegar, D. Momodu, J. Dangbegnon, F. Taghizadeh, N. Manyala, Electrochim Acta. **151**, 386 (2015)
58. F. Lufrano and P. Staiti, *Mesoporous Carbon Materials as Electrodes for Electrochemical Supercapacitors* (2010).
59. S.S. Karade, A. Agarwal, B. Pandit, R.V. Motghare, S.A. Pande, B.R. Sankapal, J. Colloid. Interface. Sci. **535**, 169 (2019)
60. S. Alkhalaf, C.K. Ranaweera, P.K. Kahol, K. Siam, H. Adhikari, S.R. Mishra, F. Perez, B.K. Gupta, K. Ramasamy, R.K. Gupta, J. Alloys. Compd. **692**, 59 (2017)
61. J. Xie, P. Yang, Y. Wang, T. Qi, Y. Lei, C.M. Li, J. Power Sources. **401**, 213 (2018)
62. P.I. Liu, L.C. Chung, C.H. Ho, H. Shao, T.M. Liang, M.C. Chang, C.C.M. Ma, R.Y. Horng, Desalination **379**, 34 (2016)